# Lewis Acid ($Ni^{2+}$, $Co^{2+/3+}$ or $Zn^{2+}$) modified Electron-Deficient $Ir^{4+}$ in $IrO_2$/CuO for Promoting Methane Oxidation to Ethanol and Methanol

Le Yang[1], Jinxu Huang[1], Jie Cen[2], De-Li Chen[2*], Hui Zeng[1], Zebao Rui[1*], Rafael Luque[3,4*], Peigao Duan[5]

[1] *School of Chemical Engineering and Technology, Guangdong Engineering Technology Research Center for Platform Chemicals from Marine Biomass and Their Functionalization, Sun Yat-sen University, Zhuhai 519082, China*

[2] *Key Laboratory of the Ministry of Education for Advanced Catalysis Materials, Institute of Physical Chemistry, Zhejiang Normal University, Jinhua 321004, China*

[3] *Departamento de Química Orgánica, Universidad de Córdoba, Campus de Rabanales, Edificio Marie Curie (C-3), Ctra Nnal IV-A, Km 396, E14014, Cordoba, Spain.*

[4] *Peoples Friendship University of Russia (RUDN University), 6 Miklukho-Maklaya Str.,117198, Moscow, Russia.*

[5] *Shaanxi Key Laboratory of Energy Chemical Process Intensification, School of Chemical Engineering and Technology, Xi'an Jiaotong University, No. 28, West Xianning Road, Xi'an, Shaanxi 710049, PR China.*

Email address: chendl@zjnu.cn, q62alsor@uco.es, ruizebao@mail.sysu.edu.cn

## 1.Experimental

### 1.1. Catalyst preparation

1.1.1. Synthesis of Cu-BTC

In a typical procedure, 0.08 g PVP (k-30) were dissolved in 5 mL methanol solution of trimesic acid (0.35 g) to form mixture A. Then, a 5 mL methanol solution of $Cu(NO_3)_2.3H_2O$ (0.728 g) was added into mixture A to form mixture B, which was kept stirring for 5 min before settling at room temperature for 3 h without stirring. The product was collected by centrifugation, washed several times with methanol, and dried at 60 $^oC$ overnight to obtain Cu-BTC.

1.1.2. Synthesis of M-S/Cu-BTC (M=Ni, Co or Zn)

Seed growth was realized by coating Cu-BTC with a thin layer of $MO_x$ via ultrasonication in corresponding acetate/ethanol solution, followed by calcination at 200 $^oC$ in $N_2$.

1.1.3. Synthesis of $MO_x$/CuO (M=Ni, Co or Zn)

The M-S/Cu-BTC samples were immersed in an aqueous mixture of corresponding nitrate (60 mM) and hexamethylenetetramine (60 mM) for hydrothermal treatment followed by calcination at 500 $^oC$ in air for 2 h with a ramp of 10 $^oC$/min.

1.1.4. Synthesis of $IrO_2/MO_x$/CuO (M=Ni, Co or Zn)

1 wt.% Ir was supported on $MO_x$/CuO (Ni, Co or Zn) using $H_2IrCl_6$ aqueous by wet impregnation overnight and dried, followed by calcination in air at 500 $^oC$ for 2 h with a ramp of 10 $^oC$/min. The final products were termed as $IrO_2$/NiO/CuO, $IrO_2/Co_3O_4$/CuO and $IrO_2$/ZnO/CuO, respectively.

### 1.2. Characterization of the samples

Powder X-ray diffraction (XRD) patterns were collected over the 2-theta range of 5-80$^o$ at room temperature with a Philips PW3040/60 automated diffractometer using

monochromated Cu-Kα radiation (λ= 1.5418 Å). Diffraction patterns were collected at a scanning rate of 10°/min. The surface electronic states were investigated by X-ray photoelectron spectroscopy (XPS, Thermo VG ESCALAB250 using Al Kα radiation). The XPS data were internally calibrated, fixing the binding energy of C 1s at 284.6 eV. Temperature-programmed reduction of $H_2$ ($H_2$-TPR) was conducted by gas chromatograph (GC1690) equipped with a thermal conductivity detector (TCD) in a flow of 5% $H_2$/Ar (50 ml/min) at temperatures between 40 and 600 °C with a heating rate of 10 °C/min.$CH_4$-temperature programmed reduction ($CH_4$-TPR) experiments were conducted on a chemisorption apparatus (Micromeritics Autochem 2920) connected with an online mass spectrometer (HIDEN QIC 20) to analyze the effluent gas. 100 mg of catalyst was placed in a U-shaped quartz tube and heated at a rate of 10 °C /min in a flow of 5% $CH_4$/He mixture with a flow rate of 30 mL/min. Before measurement, the catalyst was first heated to 200 °C in He for 30 min to remove the surface adsorbates. Bronsted and Lewis acidity of the samples was investigated by FTIR spectroscopy of adsorbed pyridine. FTIR spectra were recorded in a Bruker Vertex spectrometer in adsorbance mode. In a typical experiment, a sample was pressed into a self-supporting wafer with a density of 5-6 mg cm-1. The wafer was placed in a controlled-environment transmission cell equipped with $CaF_2$ windows. Prior to recording the spectra, the sample was evacuated to $10^{-3}$ Pa at 200 $^{o}$C for 1 h to remove surface molecules and cooled to room temperature in vacuum. The sample was then exposed to 2.67 Pa pyridine and kept for 30 min before temperature was raised to 40 $^{o}$C. After a hold time of 30 min, the sample was evacuated to $10^{-3}$ Pa and held for 30 min. Then the spectrum was recorded. The gas products in the head space of the reactor is collected and $C_2H_4$ was identified using Hiden HPR-20 mass spectrometer (MS).

**1.3. Catalytic activity tests**

Typically, 10 mg catalyst and 30 mL deionized water was loaded in a 100 mL reactor with PTFE lining (Anhui Kemi Machinery Technology Co., Ltd., Anhui, China; Model MS100-P5-T4-HC1-SV). All parts of the autoclave that directly contacted the reactants were made of Hastelloy. Batch reactor-tests were conducted at a fixed methane pressure of 3 bar and 1 bar air at 150 $^{o}$C with a reaction time of 3 h unless otherwise specified. All the feedstock components refer to the initial loading at room temperature. After the reaction, the reactor was cooled to room temperature naturally and the liquid product was filtrated through a 0.22 μm filter using a syringe before collected in a GC vial for further analysis. The effect of $CH_4$ feeding pressure was checked with the reaction conditions: various $CH_4$ feeding pressure, 1 bar air, 30 mL water, 150 $^{o}$C and reaction time of 3 h.

**1.4. Product analysis**

The liquid product was first analyzed using Bruker 600 MHz $^{1}$H-NMR and $^{12}$C-NMR. The main products in liquid are methanol and ethanol, and side product is acetaldehyde. These compounds were further checked by comparing their GC signals with those of the model compounds. Quantitative analysis was performed using a Shimadzu GC-2030 equipped with a 50 m×0.2 mm×0.33 μm HP-5 capillary column, a flame ionization detector (FID), and an autoinjector. External standard method was used for the quantification. Each single data point was measured by repeating three times under the same condition. Selectivity of methanol was calculated as (mole of $CH_3OH$)/(total carbon mole of liquid products)×100%. Selectivity of ethanol was calculated as (mole of $C_2H_5OH$)×2/(total carbon mole of liquid products)×100%. $C_{alcohol}$ was calculated as (mole of $CH_3OH$) + (mole of $C_2H_5OH$).

**1.5 Theoretical Details and Models**

All of the calculations were performed using density functional theory with Perdew-

Burke-Ernzerhof (PBE)[1] functional combined with the Grimme's corrections for the dispersion energy, *i.e.*, PBE-D3,[2] as implemented in VASP code.[3-6] The spin-polarized DFT calculations were carried out with a plane-wave expansion cutoff of 500 eV for all of the structural optimizations until the force for each ion is less than 0.05 eV/Å. The $IrO_2$ bulk was optimized via full relaxation with 9×9×12 Monkhorst-Pack *k*-point, leading to the optimized lattice parameters of $a$ = 4.48 and $c$ = 3.17 Å, in good agreement with the experimental values of 4.50 and 3.16 Å. In order to uncover the active sites for the formation of methanol and ethanol on $IrO_2$/CuO/ZnO samples, different theoretical models were built to illustrate the reaction mechanism. The $IrO_2$(110) surface was considered as the active surface for the activation of $CH_4$,[7] herein, the surface was modeled by a 4×2 unit cells with a corresponding 2×2×1 Monkhorst-Pack *k*-point mesh. The model consists of 144 atoms. Three layers was modeled to represent the (110) surface with the top two layers allowed to fully relax during the calculations, and the vacuum was set to at least 12 Å. There are coordinatively unsaturated (cus) metal sites on the surface of $IrO_2$(110), labeled as $Ir_{cus}$, and O atoms occupy the bridge sites ($O_{br}$) that connect two Ir sites, as shown in Figure S5. The adsorbed O atoms (either from $O_2$ or $H_2O$) occupy the on-top sites above $Ir_{cus}$ sites are labeled as $O_t$. The $Ir_{cus}$ sites were considered as the active adsorption sites for $CH_4$ molecules. The climbing image nudged elastic band (CI-NEB) method[8] was used to search the transition states, which were further confirmed by performing the frequency calculations.

The bulk ZnO (Figure S6) was computed using PBE-D3 functional with

Monkhorst-Pack k-point of 11×11×9, and the optimized lattice parameters are $a$ = 3.27, $c$ = 5.23 Å, $\gamma$ = 120, in good agreement with experimental values of $a$ = 3.25, $c$ = 5.21 Å.[8] The ZnO(100) surface was modeled using six layers slab and a supercell of 3×2 unit cells with vacuum at least 12 Å, and the top three layers were fully relaxed during all of the structural optimizations until the force on each ion is less than 0.05 eV/Å. The model consists of 72 atoms. The Monkhorst-Pack k-point of 2×2×1 was used to model the slab, and the kinetic cutoff of 500 eV was adopted.

The $Co_3O_4$(110) was adopted as the model to represent $Co_3O_4$ surface. The (110) surface has two different termination, *i.e.*, (110)-A termination surface with two types of cations ($Co^{2+}$ and $Co^{3+}$) and one type of anion (Oxygen atom with 3-fold coordination) and (110)-B termination with only one type of cation ($Co^{3+}$) and two types of anions (Oxygen atoms with 2 and 3 fold coordination). The (110)-B was suggested to be more stable and thus it is used in this study (as shown in Figure S7). The on-site Coulomb repulsion correction term of $U$ within the Hubbard scheme (PBE+$U$) was used in the 3d electrons of Co. The effective $U_{eff}$ value ($U$-$J$) was set to 2.0 eV.[9] The conventional unit cell was optimized with kinetic cutoff energy of 500 eV using 3×3×3 k-point mesh sampling, and the obtained lattice parameter constant of 8.09 Å is in good agreement with the experimental value of 8.07 Å.[10] The $Co_3O_4$(110) surface was modeled by $p$(2×1) with vaccum of 12 Å, and the surface contains 6 layers with the top three layers fully relaxed and the bottom three layers fixed during all of the calculations. The Monkhorst-Pack k-point of 2×2×1 was used to model the slab, and the kinetic cutoff of 500 eV was used. The Grimme's correction (D3) was applied to

account for the dispersion energy of species on the surface.

The bulk NiO was optimized using PBE+U with $U_{eff}$ = 6.45 eV, [11] and the optimized lattice parameter constant was calculated to be 4.17 Å with 9×9×9 k-poing mesh sampling, which is in good agreement with experimental value of 4.17 Å.[12] In this work, NiO(111) is not the major surface and is a second major surface (Figure 1a). However, the NiO(111) has been considered as a typical surface for NiO since it has been reported to adsorb substrates such as water vapor,[11] which dissociates rapidly on the NiO(111) surface investigated by DFT method. Therefore, the NiO(111) surface is adopted. The antiferromagnetic NiO(111) surface was model with 7 layers (Figure S7) and the top four layers were allowed to fully relax and the bottom three layers were fixed during the calculations. The Monkhorst-Pack k-point of 2×2×1 was used to model the slab, and the kinetic cutoff of 500 eV was used. The Grimme's correction (D3) was applied to account for the dispersion energy of species on the surface.

Since the CuO(111) is the most stable CuO facet and thus it was used to represent the CuO surface in this study. The effective $U_{eff}$ value of 4.0 eV was applied to simulate CuO.[13, 14] The bulk CuO with lattice parameter constants of a = 4.65 Å, b = 3.41 Å, c = 5.11 Å (Figure S7) was used to build the CuO(111) slab consists of 9 layers with the top five layers fully relaxed and the bottom four layers fixed during the calculations. The Monkhorst-Pack k-point of 2×2×1 was used to model the slab, and the kinetic cutoff of 500 eV was used. The Grimme's correction (D3) was applied to account for the dispersion energy of species on the surface.

Table S1. Metal composition evaluated by XPS analysis.

| Catalyst | Ir | Cu | Zn/Co/Ni |
|---|---|---|---|
| | wt.% | | |
| $IrO_2/ZnO/CuO$ | 1.1 | 28.8 | 15.3 |
| $IrO_2/Co_3O_4/CuO$ | 1.2 | 31.5 | 16.1 |
| $IrO_2/NiO/CuO$ | 1.1 | 27.3 | 9.7 |

Table S2. Concentration of Brønsted and Lewis acid sites (IR spectroscopy of adsorbed pyridine at 40 °C).

| Catalyst | BAS (μmol/g) | LAS (μmol/g) | (LAS-BAS)/LAS | |
|---|---|---|---|---|
| | | | 40 °C | 150 °C |
| $IrO_2/ZnO/CuO$ | 3.1 | 45.4 | 0.93 | 0.88 |
| $IrO_2/Co_3O_4/CuO$ | 6.1 | 63 | 0.90 | 0.85 |
| $IrO_2/NiO/CuO$ | 32.7 | 228.4 | 0.86 | 0.73 |
| $IrO_2/CuO$ | 8.9 | 37.8 | 0.77 | 0.62 |

Table S3. Concentration of Brønsted and Lewis acid sites of $IrO_2/ZnO/CuO$ with different loading of Zn (IR spectroscopy of adsorbed pyridine at 40 °C).

| Zn(wt.%) in $IrO_2/ZnO/CuO$ | BAS (μmol/g) | LAS (μmol/g) | (LAS-BAS)/LAS | |
|---|---|---|---|---|
| | | | 40 °C | 150 °C |
| 15.3 | 3.1 | 45.4 | 0.93 | 0.88 |
| 6.6 | 4.5 | 42.4 | 0.89 | 0.81 |
| 2.7 | 5.6 | 39.8 | 0.86 | 0.73 |
| 0 | 8.9 | 37.8 | 0.77 | 0.62 |

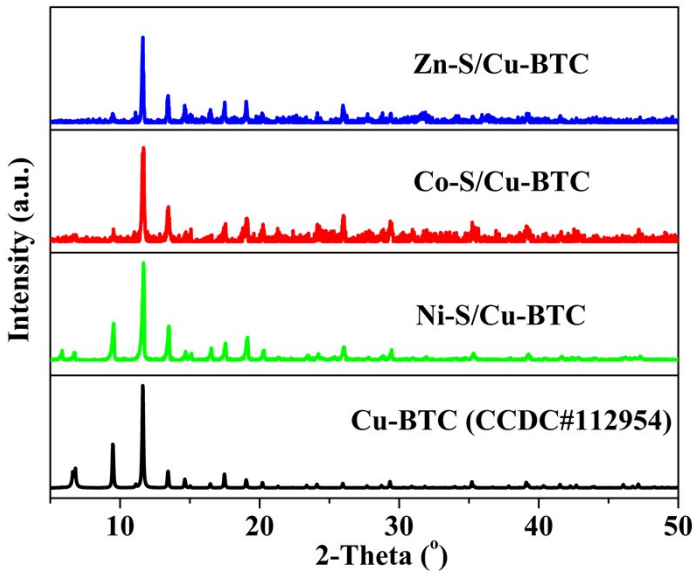


Figure S1. XRD patterns of the corresponding samples after seed growth.

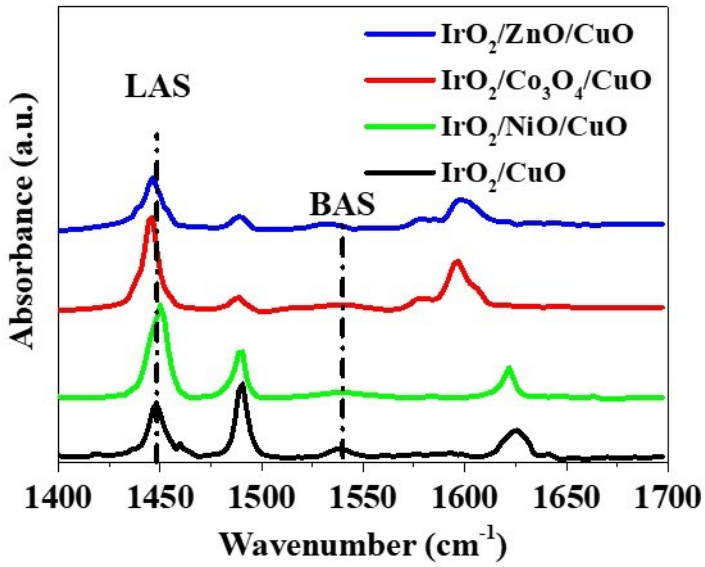


Figure S2. FT-IR spectra of pyridine desorption at 40°.

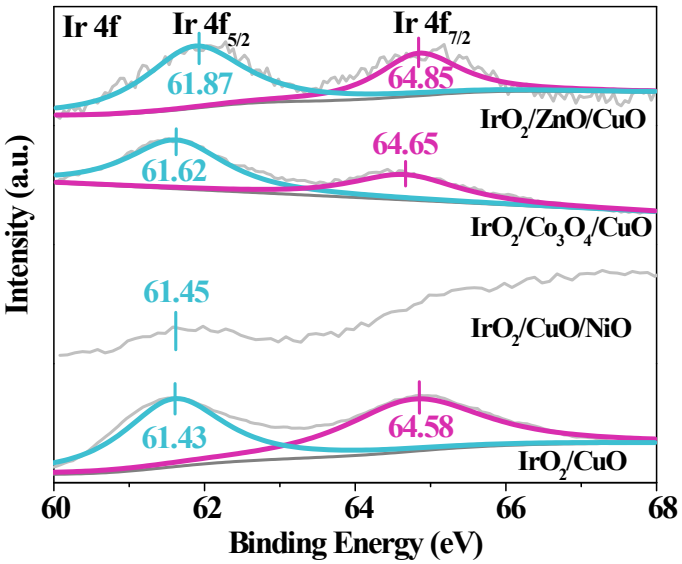


Figure S3. XPS spectra of Ir 4f on the samples.

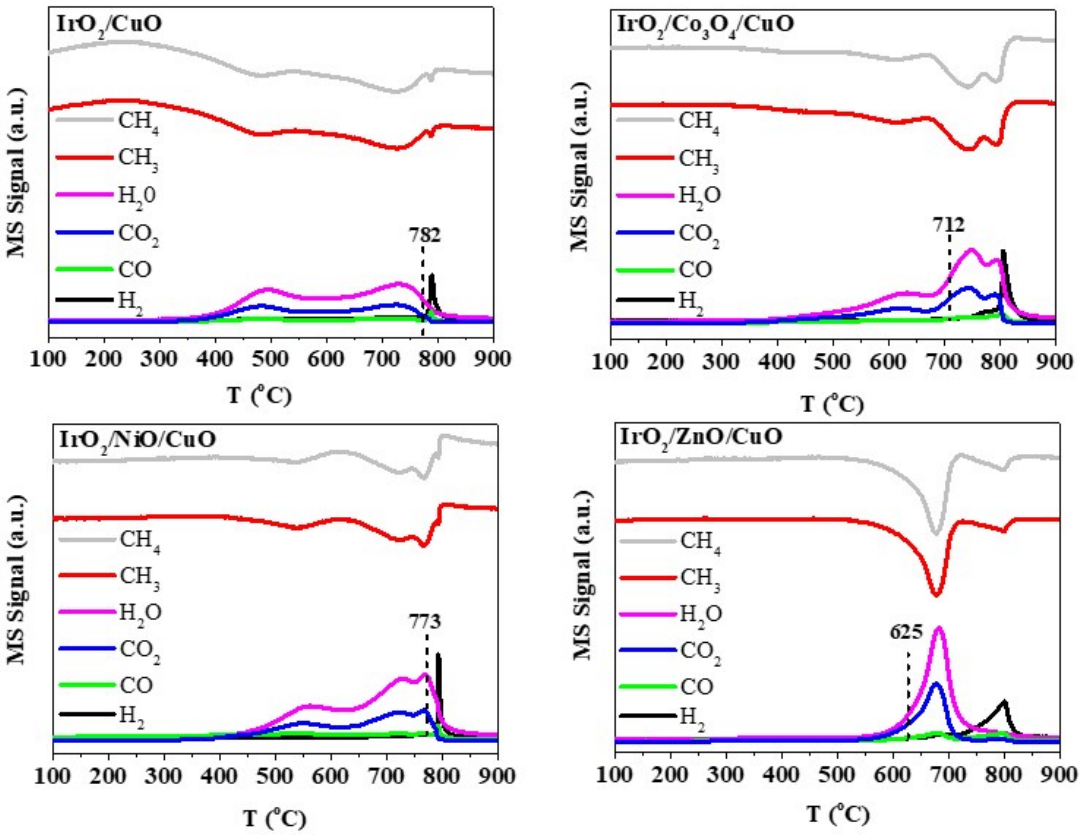


Figure S4. $CH_4$-TPR-MS profiles of the samples.

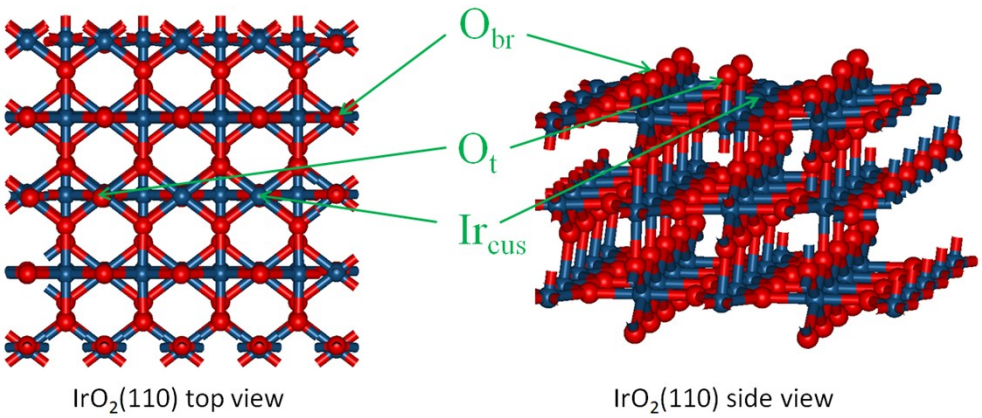


Figure S5. The top and side views of the model representations for $IrO_2$(110) surface. The Ir and O atoms are represented by blue and red balls, respectively. $O_t$: top site, $O_{br}$: bridge site.

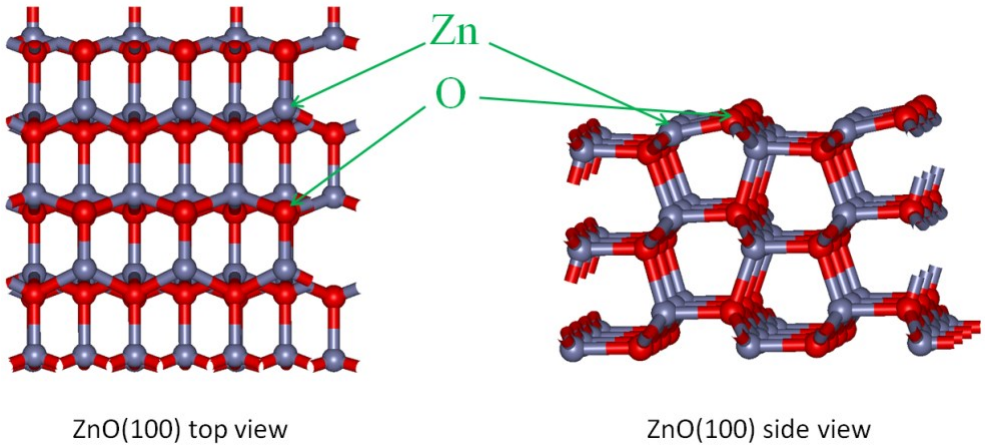


Figure S6. The top and side views of the model representations for ZnO(100) surface. The Zn and O atoms are shown by gray and red balls, respectively.

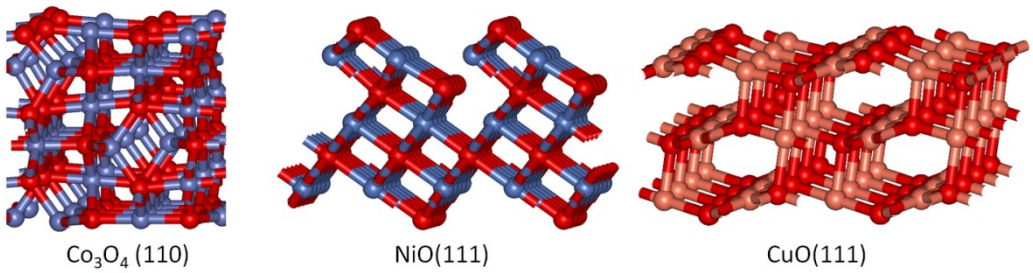


Figure S7. The models of $Co_3O_4$(110), NiO(111), and CuO(111) surfaces.

## 2. Discussion

### 2.1 Activation of $CH_4$ molecule

The calculations indicate that there is a large difference of the $CH_4$ dissociation on $IrO_2$(110) and ZnO(100). As shown in Figure S8, the energy barrier is 0.36 eV on $IrO_2$(110), and the dissociation process is exothermic with a value of 0.90 eV. However, on ZnO(100) surface, the $CH_4$ activation pathway accompanies with a larger energy barrier of 2.29 eV, indicating it is dynamically very difficult for the activation of $CH_4$ molecule on ZnO(100) surface. Therefore, it is reasonable to expect that the $IrO_2$ particle is the activation sites for $CH_4$.

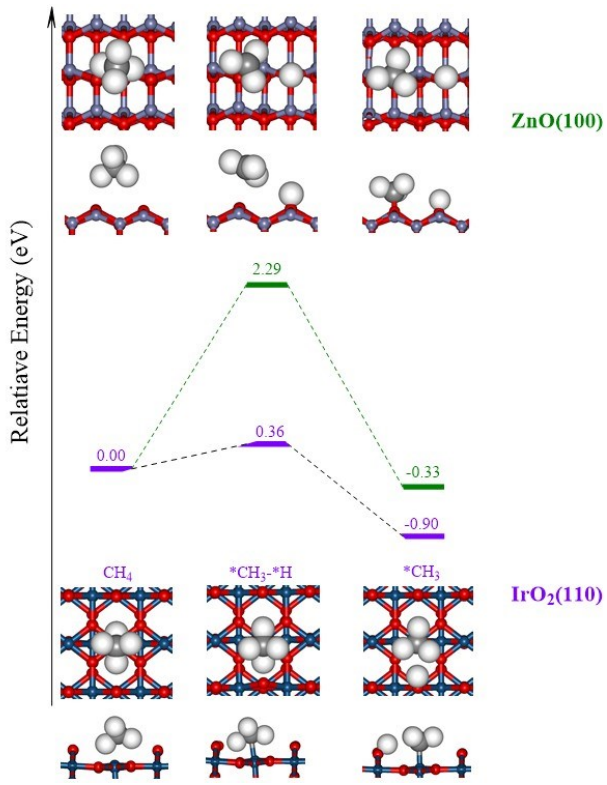


Figure S8. The comparison of the $CH_4$ activation pathways on $IrO_2$(110) and ZnO(100).

### 2.2 Stabilities of different species such as $H_2O$, $O_2$, *O, and *OH on the surfaces of $IrO_2$(110) and ZnO(100).

As shown in Figure S9, the $O_2$ molecule is adsorbed with a side-on configuration on the top of two neighboring $Ir_{cus}$ sites ($*O_2$). The computed binding energy for the $O_2$

molecule is -2.01 eV (more negative value means stronger binding), and the O-O distance is 1.40 Å, larger than the corresponding bond distance of 1.20 Å for $O_2$ gas molecule, indicating the adsorbed $O_2$ gas is activated on the surface of $IrO_2(110)$. Furthermore, the dissociation energy of the adsorbed $O_2$ was computed to be only 0.16 eV, forming two isolated active O (or $O_t$) sites on the top site of $Ir_{cus}$, which is lower in energy than the $*O_2$ state (see Figure S9) by 0.22 eV. The obtained active $O_t$ sites could be treated as the sites for the formation of methanol.

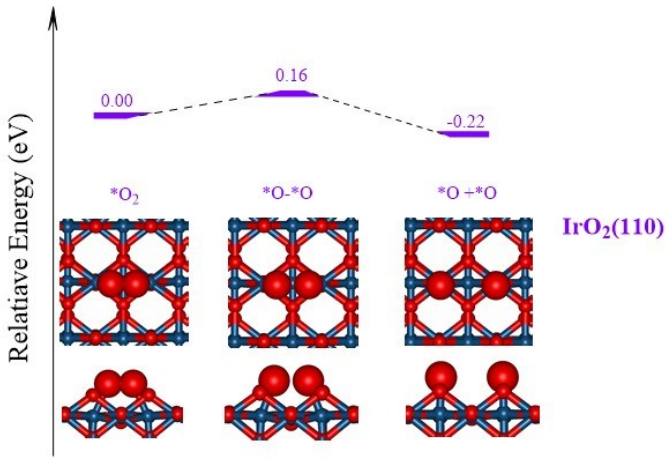


Figure S9. The dissociation pathway of $O_2$ on $IrO_2(110)$ surface.

The other source of active $O_t$ sites is from the dissociation of $H_2O$ molecule on the surface of $IrO_2(110)$. As shown in Figure S10, the $H_2O$ molecule is adsorbed at the $Ir_{cus}$ site with a binding energy of -1.72 eV, and the dissociation of $H_2O$ is barrierless and the dissociation process is exothermic by 0.23 eV. The adsorbed *OH group on the $Ir_{cus}$ site can be further transferred to *O ($Ir_{cus}$ site) and *H associated to the $O_{br}$ site forming $*O_{br}H$. Therefore, the O in methanol can be either from $O_2$ or $H_2O$. The energy barrier for the H transfer between the $O_t$ and $O_{br}$ is about 0.17 eV, and thus both $*O_tH$ and $*O_{br}H$ should be available on the $IrO_2(110)$ surface.

As a comparison, the binding energy for $H_2O$ on ZnO(100) is about -0.75 eV, much

weaker than that (-1.72 eV) on $IrO_2(110)$ surface. The calculations show that the dissociation of $H_2O$ molecule on ZnO(100) is endothermic with a value of 0.65 eV (see Figure S10), and the energy barrier for the dissociation is 0.73 eV, much higher than that on $IrO_2(110)$, suggesting that the $H_2O$ molecule is adsorbed on the ZnO(100) surface with a moderate binding strength. Therefore, the adsorbed $H_2O$ is thermodynamically stable on ZnO(100), while the $H_2O$ molecule is both thermodynamically and dynamically unstable on $IrO_2(110)$ since it tends to dissociate into active species such as *O or *OH group. This explains why it is the active $O_t$ (or $O_tH$) involves in the formation of $CH_3OH$ rather than the $H_2O$ molecule on $IrO_2(110)$ surface. While on ZnO(100) surface the adsorbed $H_2O$ molecule directly reacts with the adsorbed $C_2H_4$ forming $C_2H_5OH$ (Figure 4).

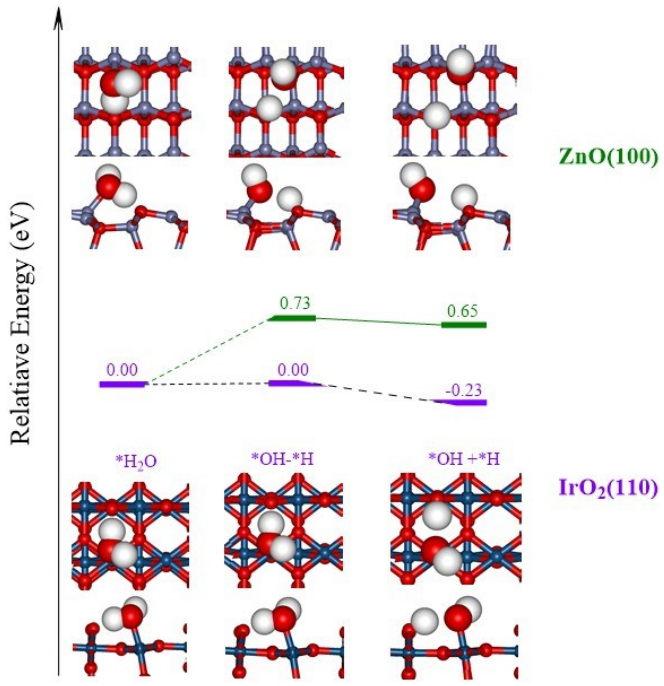


Figure S10. The comparison of the pathways for the dissociation of $H_2O$ molecules on the $IrO_2(110)$ surface and ZnO(100) surface.

**2.3 Competitive Reaction Pathways on $IrO_2(110)$**

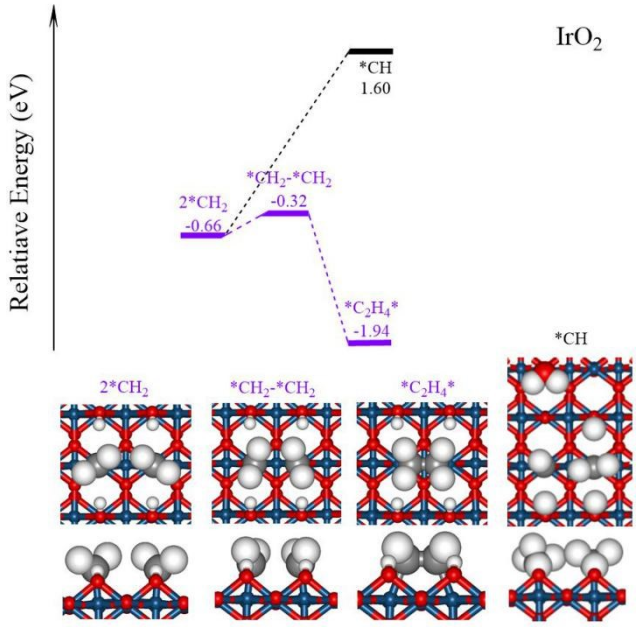


Figure S11. Comparison of the competing reaction pathways starting from 2*$CH_2$.

It is noted that the further dehydrogenation of *$CH_2$ (see structure of 2*$CH_2$ in Figure S11) to *CH is thermodynamically unfavorable since the process is endothermic by 2.26 eV, with the dehydrogenated H attacking the nearby OH group forming $H_2O$ molecule. In contrast, the pathway for ethylene formation from 2*$CH_2$ overcomes a much less energy barrier (Figure S11). Therefore, the further dehydrogenation of $CH_2$ is not considered in this work.

As shown in Figure S12 for the *$C_2H_4$* state, the two C atoms strongly bonds to two $Ir_{cus}$ sites, leading to a large desorption energy of 1.46 eV for the formation of the gas $C_2H_4$. The obtained $C_2H_4$ could either adsorb on ZnO and $IrO_2$ particles, which will form different products. The *$C_2H_4$* state can be hydrogenated to *$C_2H_5$ with an energy barrier of about 1.41 eV, which is competitive to the desorption energy (1.46 eV). However, the energy barrier to the adsorbed ethanol state (*$OHC_2H_5$) has a much higher value of 2.28 eV, indicating the generation of ethanol on $IrO_2$(110) is less competitive

than the reaction pathways to gas $C_2H_4$.

The two possible reaction pathways for the ethanol formation are compared, as shown in Figure S12. The $*CH_3$ can either react with the $O_t$ or $O_tH$ species on $IrO_2(110)$, and the former pathway involves two steps with the kinetic energy up to 1.06 eV, smaller than the latter pathway with kinetic energy of 1.35 eV. Since both $O_t$ and $O_tH$ species are available on $IrO_2(110)$ as discussed above, the $*CH_3$+$*O_t$ pathway should be the dominant reaction and then the obtained $*OCH_3$ accepts H from $H_2O$ forming the adsorbed methanol state ($*OHCH_3$). As the latter pathway only cost 0.29 eV more kinetic energy, indicating methanol can also be produced via $*CH_3$ +*OH pathway.

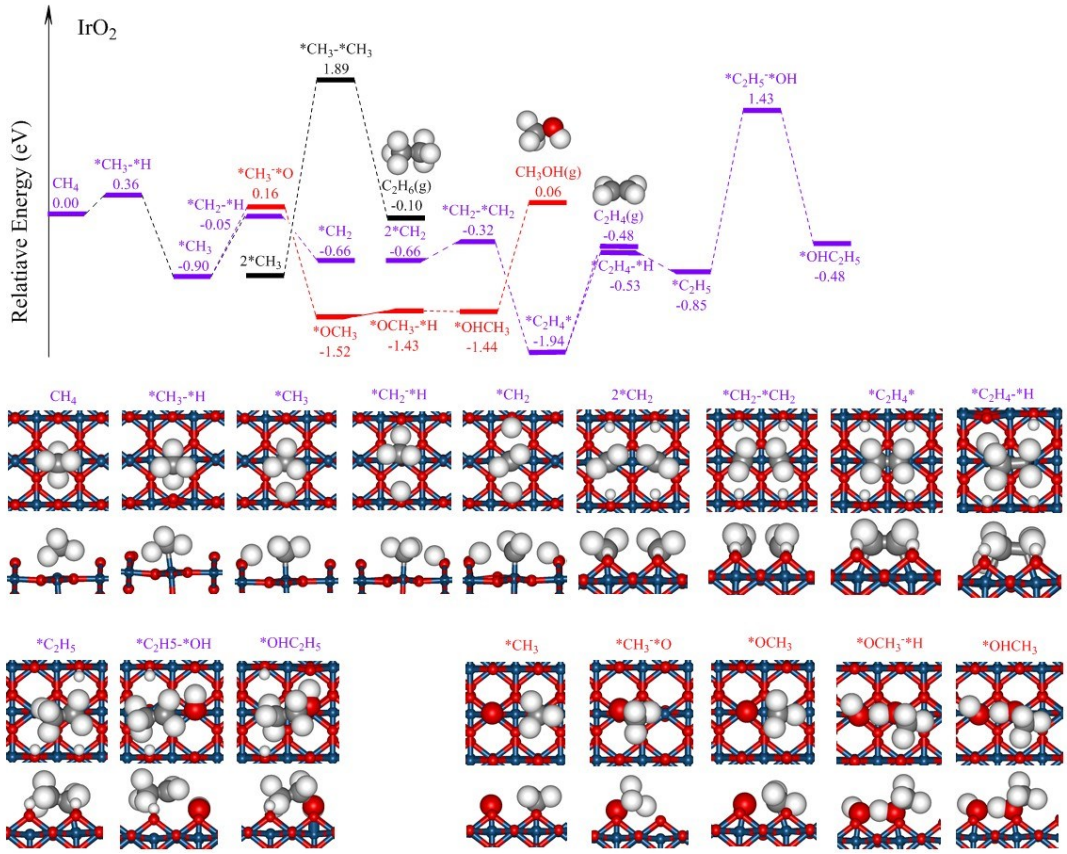


Figure S12. Several competitive reaction pathways on $IrO_2(110)$. The purple color represents the reaction pathways to the formation of $C_2H_4$ gas and $C_2H_5OH$; the red

color shows the formation of $CH_3OH$; the black color is for the formation of $C_2H_6$. The top and side views of the structures are shown for the initial states, intermediate states, and final states.

## 2.4 The Reaction Pathways on ZnO(100) surface

The complete reaction pathways and the structures of different states were summarized in Figure S13. The reaction starts from the adsorbed ethylene state (*$C_2H_4$*), where the two C atoms binding to O and Zn, respectively, with an adsorption energy of -0.36 eV. With the adsorbed $H_2O$ molecule at neighboring site, the C-Zn bond was activated by transferring H atom from $H_2O$ to the formation of *$C_2H_5$ state with an energy barrier of 0.63 eV. There are two pathways to proceed, one is the O-Zn cleavage and the other is the direct formation of *$OHC_2H_5$, the former leads to an upright configuration of *$OC_2H_5$ state and thus O vacancy is formed, while the latter is a process with $C_2H_5$ group moving towards the *OH group nearby forming *$OHC_2H_5$(1) state. Apparently, the O-Zn cleavage undergoes a much lower energy barrier of only 0.72 eV and then proceed to accept another H from $H_2O$, giving rise to the formation of *$OHC_2H_5$. The desorption energy of 1.20 eV for the $C_2H_5OH$ from the ZnO(100)

surface is also smaller than those for methanol and ethylene on $IrO_2$(110). Therefore, the formation of ethanol is dynamically competitive on ZnO(100) surface compared to that on $IrO_2$(110) surface.

2.5 The O-M bond cleavage on different $MO_x$ surfaces

Since the gas $C_2H_4$ adsorption on $Co_3O_4$(110), NiO(111), and CuO(111) surfaces have a similar structure compared to ZnO(100), *i.e.*, the two C atoms of $C_2H_4$ bond to lattice O and Metal, respectively, and thus we performed calculations for the O-Metal bond cleavage on various $MO_x$ surfaces to evaluate the formation of ethanol. As shown in Figure 4C, the energy barriers on ZnO(100), $Co_3O_4$(110), NiO(111), and CuO(111) surfaces are 0.72, 1.08, 1.29, and 1.58 eV, respectively, in line with the experimental ethanol yield sequence of $IrO_2$/ZnO/CuO> $IrO_2$/$Co_3O_4$/CuO> $IrO_2$/NiO/CuO> $IrO_2$/CuO. The excellent agreement between the theory and experiments further confirm that the formation of ethanol should occur on the $MO_x$ surfaces.

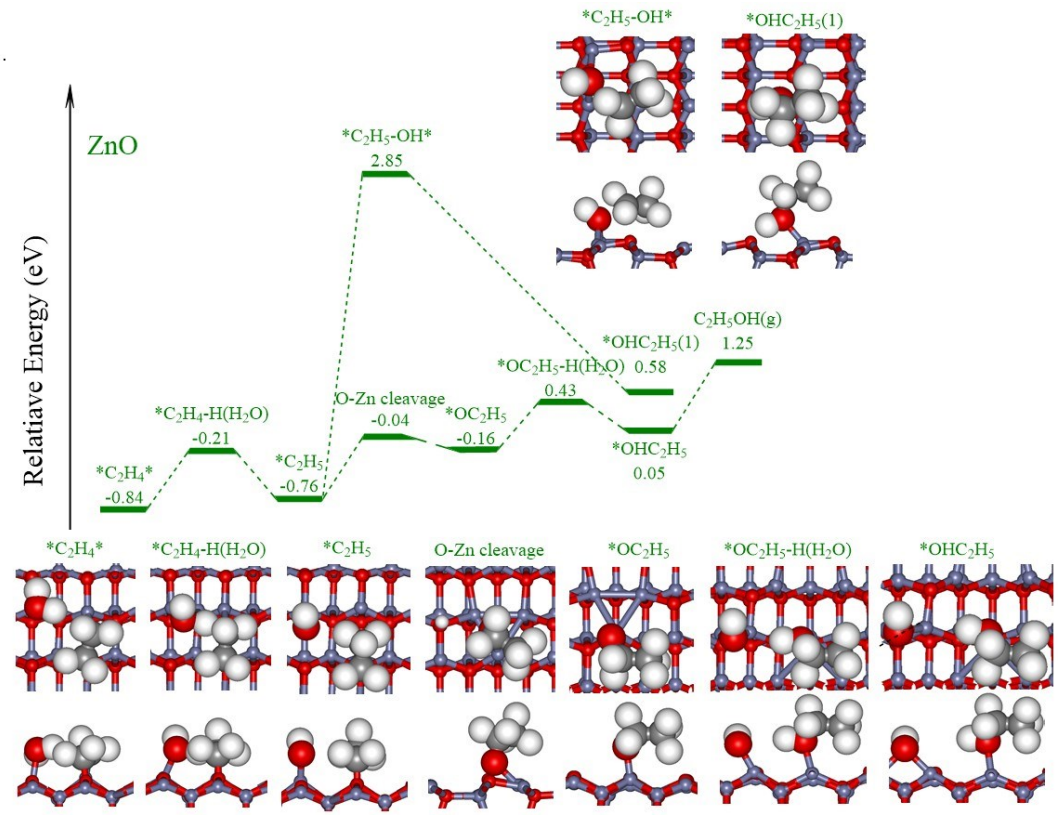


Figure S13. The complete pathways for the formation of $C_2H_5OH$ on ZnO(100), as well as the top and side views of the structures for different states.

**References:**

1. Perdew, J. P.; Burke, K.; Ernzerhof, M. Generalized Gradient Approximation Made Simple. *Phys. Rev. Lett.* **1996**, *77*, 3865−3868.

2. Grimme, S.; Antony, J.; Ehrlich, S.; Krieg, S. A Consistent and Accurate Ab Initio Parameterization of Density Functional Dispersion Correction (DFT-D) for the 94 Elements H-Pu. *J. Chem. Phys.* **2010**, *132*, 154104.

3. Kresse, G.; Furthmüller, J. Efficient Iterative Schemes for Ab Initio Total-Energy Calculations using a Plane-Wave Basis Set. *Phys. Rev. B: Condens. Matter Mater. Phys.* **1996**, *54*, 11169−11186.

4. Kresse, G.; Furthmüller, J. Efficiency of Ab-Initio Total Energy Calculations for Metals and Semiconductors using a Plane-Wave Basis Set. *Comput. Mater. Sci.* **1996**, *6*, 15−50.

5. Kresse, G.; Hafner, J. Ab Initio Molecular-Dynamics Simulation of the Liquid-Metal-Amorphous-Semiconductor Transition in Germanium. *Phys. Rev. B: Condens. Matter Mater. Phys.* **1994**, *49*, 14251−14269.

6. Kresse, G.; Hafner, J. Ab Initio Molecular Dynamics for Liquid Metals. *Phys. Rev. B: Condens. Matter Mater. Phys.* **1993**, *47*, 558−561.

7. Kim, M.; Franklin, A.; Martin, R.; Feng, F.; Li, T.; Liang Z.; Asthagiri, A.; Weaver, J. F. Adsorption and Oxidation of $CH_4$ on Oxygen-Rich IrO2(110). *J. Phys. Chem. C* **2019**, *123*, 27603-27614.

8. Yang, Z.; Xiong, S.-J. Adsorption of Ag and Au Atoms on Wurtzite ZnO(0001) surface, *Surf. Sci.* **2011**, *604*, 40-45.

9. Hu, W.; Lan, J.; Guo, Y.; Cao, X.-M.; Hu, P. Origin of Efficient Catalytic Combustion of Methane over $Co_3O_4$(110): Active Low-Coordination Lattice Oxygen and Cooperation of Multiple Active Sites, *ACS Catal.* **2016**, *6*, 5508-5519.

10. Hu, L.; Peng, Q.; Li, Y. Selective Synthesis of $Co_3O_4$ Nanocrystal with Different Shape and Crystal Plane Effect on Catalytic Property for Methane Combustion, *J. Am. Chem. Soc.* **2008**, *130*, 16136−16137.

11. Zhao, W.; Bajdich, M. Carey, S.; Vojvodic, A.; Nørskov, J. K.; Campbell, C. T. Water Dissociation Adsorption on NiO(111): Energetics and Structure of the Hydroxylated Surface, *ACS Catal.* **2016**, *6*, 7377-7384.

12. Sawatzky, G. A.; Allen, J. W. Magnitude and Origin of the Band Gap in NiO, *Phys. Rev. Lett.* **1984**, *53*, 2339.

13. Song, Y.-Y.; Wang, G.-C. A DFT Study and Microkinetic Simulation of Propylene Partial Oxidation on CuO(111) and CuO(100) Surfaces, *J. Phys. Chem. C*, **2016**, *120*, 27430-27442.

14. Åsbrink, S.; Norrby, L.-J. A Refinement of the Crystal Configuration of Copper(II) Oxide with a Discussion of Some Exceptional E.S.D.'S. *Acta Crystallogr., Sect. B: Struct. Crystallogr. Cryst. Chem.* **1970**, *26*, 8-15.